MATERIALS CHEMISTRY FRONTIERS

CHINESE CHEMICAL SOCIETY

ROYAL SOCIETY OF CHEMISTRY

RESEARCH ARTICLE

View Article Online
View Journal | View Issue

Cite this: *Mater. Chem. Front.*, 2024, **8**, 1611

Robust imidazole-linked Ni-phthalocyanine-based covalent-organic framework for CO_2 electroreduction in the full pH range†

Xu Yang,[ac] Duan-Hui Si,*[a] Hong-Fang Li,[a] Rong Cao *[abd] and Yuan-Biao Huang *[abd]

The electroreduction of CO_2 to value-added chemicals is a promising approach to utilize CO_2 and mitigate greenhouse gas emission. Covalent organic frameworks (COFs) with abundant accessible active sites, tunable pore size, and large CO_2 adsorption capacity are considered promising electrocatalysts for CO_2 conversion. However, most COFs linked by reversible covalent bonds exhibit poor stability, which limits their application for CO_2 electroreduction reactions in acidic or alkaline electrolytes. Herein, a Ni-phthalocyanine-based COF linked by stable imidazole building blocks, named NiPc-Im-COF, was synthesized through the condensation reaction of 2,3,9,10,16,17,23,24-octa-aminophthalocyaninato Ni(II) and 4,4′-biphenyl dialdehyde. The obtained NiPc-Im-COF exhibits high chemical stability after soaking in concentrated HCl and KOH. When applied for the electroreduction of CO_2, the NiPc-Im-COF exhibits high CO selectivity (>90%) in electrolytes with different pH values. Specifically, the NiPc-Im-COF shows a high CO partial current density of 267 mA cm^{-2} with a CO selectivity of 90% at −0.8 V *vs.* the reversible hydrogen electrode (RHE) in 5 M KOH solution, and meanwhile, over 90% of FE_{CO} and 6 hours of stability at −1.3 V in 0.5 M K_2SO_4 (pH = 1). The XRD patterns prove that the structure of the NiPc-Im-COF is not destroyed after CO_2 electroreduction at different pH values. This work presents a strategy to improve the stability of COFs *via* irreversible covalent linkage and offers an efficient CO_2RR in the full pH range, which paves a new pathway for the industrial application of COFs in CO_2 electroreduction.

Received 8th November 2023,
Accepted 27th January 2024

DOI: 10.1039/d3qm01190a

rsc.li/frontiers-materials

Introduction

Today, with the excessive use of fossil fuels, the rapid increase in the content of CO_2 in the atmosphere has led to a series of problems, including global warming and rising sea levels.[1–3] Various approaches, including photocatalysis, electrocatalysis, and thermal catalysis, have been explored to address this challenge.[4–10] Among these methods, the electrocatalytic reduction of CO_2 to fossil fuels driven by renewable energy could realize the recycling of carbon resources.[11,12] Nowadays, many kinds of electrocatalysts, including metal-based catalysts (Sn-, Ag-, and Cu-based catalysts); Fe-, Co-, Ni-based single-atom catalysts; and metal-free catalysts, were employed to promote the CO_2 electroreduction reaction (CO_2RR) and produce diverse chemicals and fuels, including CO, HCOOH, CH_4, and C_2H_4.[13–23] However, many problems remain to be solved in the CO_2RR, such as ambiguous active centers led by complex composition, low stability due to reconstruction of catalysts, low selectivity resulting from a multi-electron transfer process, and the competitive hydrogen evolution reaction (HER).[24–29] Hence, it is necessary to design highly efficient electrocatalysts with clear active centers. In addition, as is well known, to achieve highly efficient CO_2RR performance with high current density, alkaline and/or acidic electrolytes are usually required. Under alkaline conditions, CO_2 molecules readily react with OH^- and convert into carbonate/bicarbonate, which results in a low utilization of CO_2. Simultaneously, the generated carbonate/bicarbonate will block the pores of the electrode, reduce CO_2RR stability, and lead to the leakage of the electrolyte.[30] Although these problems can be avoided while using acidic electrolytes, the HER usually occurs predominantly under such conditions and far exceeds the CO_2RR. Therefore, it is

[a] *State Key Laboratory of Structural Chemistry, Fujian Institute of Research on the Structure of Matter, Chinese Academy of Sciences, Fuzhou, 350002, Fujian, China. E-mail: siduanhui@fjirsm.ac.cn, ybhuang@fjirsm.ac.cn, rcao@fjirsm.ac.cn*
[b] *Fujian Science & Technology Innovation Laboratory for Optoelectronic Information of China, Fuzhou, 350108, Fujian, China*
[c] *Fujian Cross Strait Institute of Flexible Electronics (Future Technology), Fujian Normal University, Fuzhou, 350117, Fujian, China*
[d] *University of Chinese Academy of Science, Beijing 100049, China*

† Electronic supplementary information (ESI) available. See DOI: https://doi.org/10.1039/d3qm01190a

important to develop and prepare stable electrocatalysts under such harsh conditions for the CO_2RR.

Recently, porous crystalline covalent-organic frameworks (COFs) have garnered extensive interest owing to clear and accessible active centers and diverse adjustable chemical and pore structures, which have propelled them into the spotlight within the field of electrocatalysis.[31–35] However, to obtain crystalline structures, most COFs are constructed by dynamically reversible covalent bonds, such as C=N imine bonds. These unstable bonds usually lead to the decomposition of the crystalline framework during the CO_2RR process under harsh acid or alkaline conditions.[36–40] In contrast, the construction of COFs with irreversible covalent bonds could effectively enhance their stability under acid or alkaline conditions.[41–43] Ni phthalocyanines with active sites have been shown to promote electrocatalytic CO_2RR. However, most Ni phthalocyanine-based COFs are connected with dynamic bonds such as C=N and B–O. It is still challenging to construct crystalline robust metal phthalocyanine-based COFs with irreversible covalent bonds for efficient electrocatalytic CO_2RR in gas diffusion electrodes (GDE) with acid and alkaline electrolytes. Recently, nitrogen heterocyclic units were used to construct stable COFs due to the excellent chemical stability of nitrogen heterocycles.[44,45] Herein, a Ni-phthalocyanine-based COF linked by the stable imidazole building blocks (NiPc-Im-COF) is synthesized, and the as-prepared NiPc-Im-COF exhibited high selectivity of CO (>90%) from −0.5 V to −0.8 V *vs.* reversible hydrogen electrode (RHE) and the largest CO partial current density (J_{CO}) of 267 mA cm^{-2} at −0.8 V when 5 M KOH was employed as the electrolyte in GDE. Besides, the faradaic efficiency of CO (FE_{CO}) reached 90%, and the J_{CO} arrived at 87 mA cm^{-2} at −1.4 V under the conditions of potassium sulfate aqueous solution (pH = 1). The results clearly indicate the significant potential of the stable COF connected *via* irreversible covalent bonds for the electrocatalytic CO_2RR.

Results and discussion

As depicted in Fig. 1a, NiPc-Im-COF was synthesized by the reaction of 2,3,9,10,16,17,23,24-octa-aminophthalocyaninato nickel(II) (NiPc-$(NH_2)_8$) and 4,4′-biphenyl dialdehyde (BPDH) in the mixed solvent of N-methyl pyrrolidone (NMP) and mesitylene (MT). The powder X-ray diffraction (PXRD) pattern of NiPc-Im-COF, as shown in Fig. 1b, is in agreement with the simulated profile, suggesting the formation of crystalline NiPc-Im-COF most likely with an AA stacking model (Fig. 1a). Three main peaks located at 3.55°, 7.03°, and 10.6°, could be attributed to the (100), (200), and (300) crystallographic planes, respectively. The peak at 26.6° corresponding to the (001) facet is indicative of the π–π stacking between COF layers. Notably, the main diffraction peak of NiPc-$(NH_2)_8$ in the PXRD pattern was located at 5° (Fig. S1, ESI†), which was distinct from that of NiPc-Im-COF. As demonstrated by Material Studio 7.0, the NiPc-Im-COF possessed a unit cell with dimensions $a = b =$ 25.2 Å and an interplane distance of c = 3.35 Å, in agreement

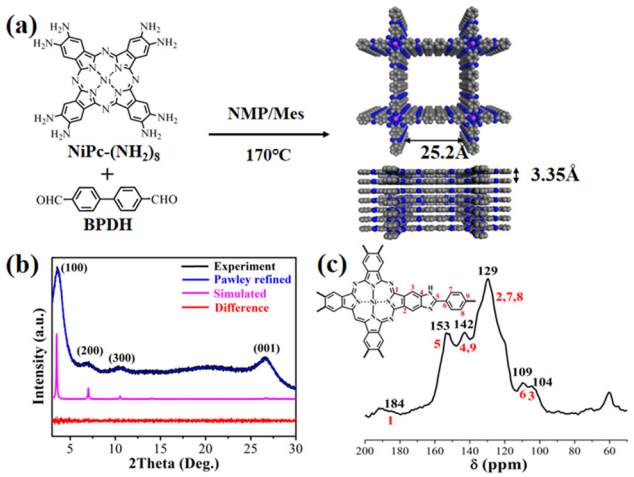

Fig. 1 (a) Schematic illustration for the synthesis of the NiPc-Im-COF, with top and side views of AA stacking. (b) Simulated and experimental NiPc-Im-COF PXRD patterns. (c) Solid-state ^{13}C NMR spectrum.

with the experimental and the resulting XRD pattern (the R_p is 1.51% and the R_{wp} is 1.64%). To provide additional validation for the successful synthesis of the COF network structure, Fourier transform infrared spectroscopy (FT-IR), and solid-state ^{13}C nuclear magnetic resonance (^{13}C NMR) spectra were performed. The FT-IR spectra (Fig. S2, ESI†) revealed the band at 1688 cm^{-1} attributed to the stretching vibration of the aldehyde-based C=O in BPDH, and the bands at 3220 cm^{-1} and 3334 cm^{-1}, signifying the vibration of –NH_2 in NiPc$(NH_2)_8$, disappeared after the reaction. Simultaneously, new bands corresponding to the C–H vibration of benzene rings emerged at 2852 cm^{-1} and 2921 cm^{-1}.[46,47] Besides, as illustrated in Fig. 1c, the solid-state ^{13}C NMR spectra of NiPc-Im-COF exhibited a special chemical shift peak at 153 ppm, which was ascribed to the C of the NH–C=N in the imidazole ring in the framework.[48] Besides, the ultraviolet-visible (UV-vis) spectra substantiate a red shift in the Q band for NiPc-Im-COF, which suggested the extended conjugation within NiPc-Im-COF (Fig. S3, ESI†). These aforementioned results indicated the successful synthesis of NiPc-Im-COF.

The scanning electron microscopy (SEM) image (Fig. 2a and Fig. S4a, ESI†) revealed that the bulk NiPc-Im-COF comprised stacked layers of nanosheets, aligning with the simulated structure. As shown in Fig. 2b and Fig. S4b, ESI,† the transmission electron microscopy (TEM) image revealed its porous structure. Additionally, high-angle annular dark-field scanning transmission electron microscopy (HAADF-STEM) and the energy-dispersive X-ray spectroscopy (EDS) elemental mapping images (Fig. 2c) illustrated the uniform distribution of C, N, and Ni elements within the NiPc-Im-COF framework, with no discernible Ni nanoparticles (Ni NPs) in TEM images, aligning with PXRD findings. At the same time, atomic force microscopy images also confirmed a sheet-like structure of NiPc-Im-COF with a height of 1.4 nm (Fig. S5, ESI†). The inductively coupled plasma (ICP) optical emission spectrometry demonstrated the Ni content of 3.75 wt% in NiPc-Im-COF, which was consistent

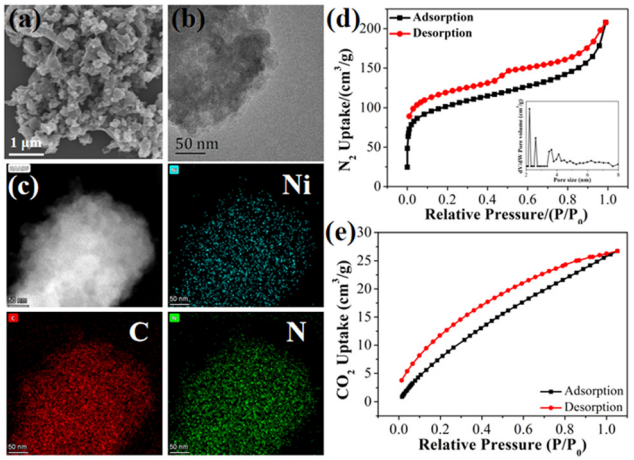

Fig. 2 (a) SEM and (b) TEM images of the NiPc-Im-COF. (c) HAADF-STEM image of the NiPc-Im-COF and elemental mapping images showing the distribution of C, N, and Ni. (d) N_2 sorption curves for the samples at 77 K. (e) CO_2 adsorption curves for the samples at 298 K.

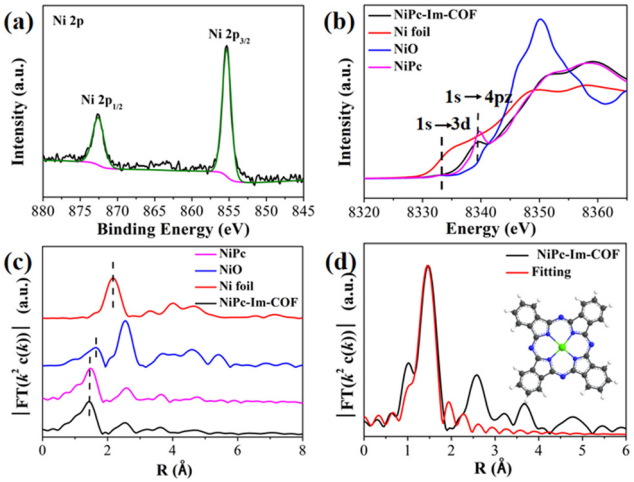

Fig. 3 (a) XPS spectra of Ni in Im-COFs; (b) the normalized Ni K-edge XANES spectra of Im-COFs, NiPc, Ni foil, and NiO; (c) Fourier transform EXAFS spectra of different samples; (d) first-shell fitting of the Fourier transformed EXAFS spectrum of Im-COFs.

with the result of EDS (Tables S1 and S2, ESI†). The porous structure of NiPc-Im-COF was investigated by N_2 adsorption–desorption experiments at 77 K. As shown in Fig. 2d and Table S3, ESI,† NiPc-Im-COF exhibited a high Brunauer–Emmer Teller (BET) surface area of 360 $m^2\ g^{-1}$ and a total pore volume of 0.32 $cm^3\ g^{-1}$. Furthermore, benefiting from the affinity of the imidazole ring for CO_2, NiPc-Im-COF displayed an impressive CO_2 uptake of 27 $cm^3\ g^{-1}$ at 298 K (Fig. 2e), highlighting its favorable CO_2 affinity, which is beneficial for enhancing the catalytic performance of CO_2RR. To evaluate the stability of NiPc-Im-COF, the NiPc-Im-COF powders were immersed in various solvents and solutions (such as *N*,*N*-dimethylformamide (DMF), ethanol (EtOH), tetrahydrofuran (THF), trichloromethane (TM) and acid/base such as concentrated HCl (1 M and 5 M), concentrated KOH (1 M and 5 M)) at room temperature for one week. As demonstrated in Fig. S6, ESI,† the PXRD patterns indicated that NiPc-Im-COF exhibited excellent acid/base and organic solvent stability. Besides, NiPc-Im-COF retained its crystallinity after soaking in THF, TM at 60 °C and DMF at 80 °C for 12 h (Fig. S7, ESI†). Additionally, the thermal stability of NiPc-Im-COF was substantiated by thermogravimetric analysis (TGA), revealing a decomposition temperature exceeding 320 °C (Fig. S8, ESI†).

X-ray photoelectron spectroscopy (XPS) survey spectrum revealed the presence of C 1s, N 1s, and Ni 2p core levels in NiPc-Im-COF (Fig. S9a, ESI†). The resonance peak of O in the spectrum might come from guest molecules in the pore or the unreacted aldehyde groups at the edge of the framework, explaining the total atomic mass fraction being less than 100%. In the high-resolution C 1s spectrum (Fig. S9b, ESI†), two prominent peaks were located at 284.8 eV and 285.97 eV, corresponding to C═C/C–C and C═N, respectively.[49–51] As shown in Fig. S9c, ESI,† the high-resolution N 1s spectrum displayed peaks at 398.6 eV and 400.16 eV. The peak at 398.6 eV was assigned to the N═C–N bond. Notably, the binding energy is at 400.16 eV, higher than that of the Ni–N bond (399.8 eV) but lower than that of the N–H bond (400.5 eV) in the imidazole ring, suggesting an interaction of Ni–N and N–H.[52–54] Moreover, the Ni 2p XPS spectrum in Fig. 3a displays two sets of peaks with binding energies of 872.7 eV and 855.4 eV for Ni $2p_{1/2}$ and Ni $2p_{3/2}$, respectively, which indicates the presence of Ni(II) species and the absence of Ni nanoparticles.[55–57] X-ray absorption spectroscopy (XAS) was performed to determine the coordination environment and electronic structure of Ni sites. As illustrated in Fig. 3b, the X-ray absorption near edge structure (XANES) exhibited nearly identical curves for NiPc-Im-COF and NiPc, indicating minimal alterations in the coordination environment and electronic structure of Ni sites. In addition, the peaks at 8334 eV and 8340 eV were detected in NiPc and NiPc-Im-COF, which could be attributed to the dipole forbidden 1s to 3d transition and the shakedown satellite 1s to 4pz transition.[58,59] The XANES curves of NiPc-Im-COF and NiPc closely resembled that of NiO. These results indicated that the valence of Ni sites in NiPc-Im-COF is approximately +2, aligning with the results of XPS. The coordination environment of the Ni sites in the NiPc-Im-COF was analyzed by extended X-ray absorption fine structure (EXAFS). As depicted in Fig. 3c, compared with Ni foil, there was no evidence of a Ni–Ni bond at 2.2 Å in NiPc-Im-COF, indicating that Ni atoms in NiPc-Im-COF existed as single Ni sites, with no presence of Ni NPs. Besides, in comparison to NiO, NiPc and NiPc-Im-COF exhibited a prominent peak at 1.4 Å, indicative of the Ni–N bond, while NiO featured a primary peak at 1.6 Å, corresponding to the Ni–O bond. These results suggest the absence of nickel oxides within NiPc-Im-COF. The EXAFS fitting was carried out to obtain the quantitative structural parameters of Ni sites in NiPc-Im-COF. As shown in Fig. 3d and Table S4, ESI,† the fitting results of NiPc-Im-COF indicated that the average coordination number of Ni–N was 4.2, further demonstrating its Ni–N_4 coordination structure.

To evaluate the CO_2RR performances of NiPc-Im-COF, the ink comprising NiPc-Im-COF and conductive carbon was drop-

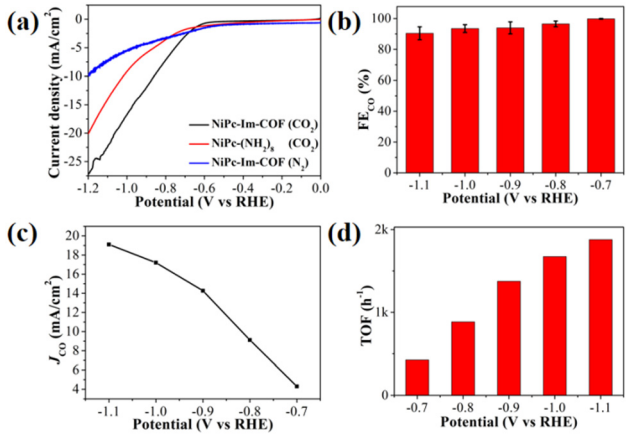

Fig. 4 The CO_2RR performances of the NiPc-Im-COF were studied in a H-cell. (a) LSV curves measured in N_2-saturated and CO_2-saturated 0.5 M $KHCO_3$ solution, scan rate = 10 mv s^{-1}; (b) FE for CO from −0.7 to −1.1 V *vs.* RHE; (c) CO partial current density; (d) TOF under different potentials.

casted on 1 cm^2 carbon paper electrode. The electrochemical tests were firstly conducted in CO_2-saturated 0.5 M $KHCO_3$ aqueous solution within a standard H-type electrochemical cell containing a two-chamber and three-electrode separated by a proton exchange membrane. Fig. 4a illustrates the linear sweep voltammetry (LSV) curves of NiPc-Im-COF, demonstrating a notably higher current density than that of conducted in the corresponding N_2-saturated electrolyte. This discrepancy suggested the CO_2RR has occurred over NiPc-Im-COF. Besides, the LSV curve of NiPc-Im-COF also displayed a superior current density than that of NiPc-$(NH_2)_8$ in CO_2-saturated 0.5 M $KHCO_3$ electrolyte, which suggested that the porosity and conductivity of NiPc-Im-COF enhance the mass and electron transfer processes, thereby increasing the current density during the electrocatalytic CO_2RR. To further assess the selectivity of NiPc-Im-COF for CO_2RR, gas chromatography (GC) was employed to detect the gas products. As shown in Fig. 4b, Fig. S12 and S13, ESI,† NiPc-Im-COF showed high faradaic efficiencies of CO (FE_{CO}) (>90%) over a wide potential range from −0.7 V to −1.1 V *vs.* reversible hydrogen electrode (RHE) and exhibited nearly 100% at −0.7 and −0.8 V. It is important to note that all the potentials mentioned in this work are referenced to the reversible hydrogen electrode (RHE). Furthermore, the CO partial current density (J_{CO}) of NiPc-Im-COF gradually increased with the rising overpotential, reaching 19.3 mA cm^{-2} at −1.1 V (Fig. 4c). Concurrently, the turnover frequency (TOF) increased with the potential and reached 1880 h^{-1} at −1.1 V. To evaluate the stability of the catalysts in 0.5 M $KHCO_3$, the time-dependent total current density curves were obtained. The long-term stability of NiPc-Im-COF was analyzed at −0.8 V in CO_2-saturated 0.5 M $KHCO_3$ (Fig. S14, ESI†). Notably, the FE_{CO} remained consistently above 90% for a duration of 20 hours. Furthermore, the PXRD pattern of NiPc-Im-COF shown in Fig. S15, ESI† remained unchanged, indicating that good crystallinity was maintained even after undergoing the CO_2 reduction reaction. Besides, the valence of Ni sites in NiPc-Im-COF was assessed by XPS after the CO_2RR in 0.5 M $KHCO_3$. The XPS curves of NiPc-Im-COF demonstrated that bonding energies at 872.7 eV and 855.4 eV are assigned to $2p_{3/2}$ and $2p_{1/2}$ of Ni(II), respectively (Fig. S16, ESI†), suggesting the excellent stability of NiPc-Im-COF under neutral condition.

To address the CO_2 mass transfer limitation in H-cells, a GDE-based alkaline flow cell was employed. The conductive ink was drop-casted on single carbon paper with an area of 0.8 cm^2 and a set of KOH solutions with gradient concentrations (1 M, 3 M, and 5 M) were used as electrolytes. As depicted in Fig. 5a, the LSV curves indicated that the total current density increased with the concentration of KOH, which resulted from the increased ion concentration and CO_2 mass transfer. The current density obtained under alkaline GDE conditions far exceeded that of the neutral H-cell. Furthermore, we conducted tests to evaluate the product selectivity under various conditions. As shown in Fig. 5b, the FE_{CO} of the catalyst maintained over 90% over a range from −0.5 V to −0.9 V under 1 M KOH. Similarly, the catalyst also showed high FE_{CO} in the presence of 3 M and 5 M KOH aqueous solutions. Furthermore, the CO partial current density of the catalyst improved significantly, with J_{CO} reaching 142 mA cm^{-2} at −0.8 V when 1 M KOH was employed as the electrolyte, which was 7-fold higher than the highest J_{CO} in 0.5 M $KHCO_3$ (Fig. 5c). Similarly, the J_{CO} also increased with the concentration of KOH (3 M and 5 M KOH) and reached 231 mA cm^{-2} and 267 mA cm^{-2} at −0.8 V (Fig. 5c),

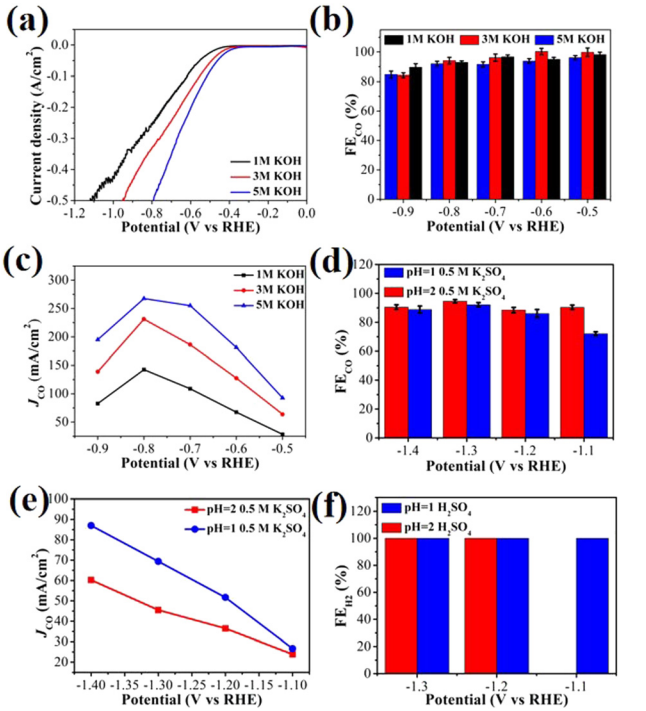

Fig. 5 CO_2RR performances for the NiPc-Im-COF were studied in a flow cell. (a) LSV curves measured in KOH solutions with a scan rate of 10 mv s^{-1}; (b) FE for CO from −0.7 to −1.1 V *vs.* the RHE and (c) CO partial current density in 1 M, 3 M, and 5 M KOH; (d) FE for CO from −1.1 V to −1.4 V *vs.* the RHE and (e) CO partial current density in 0.5 M K_2SO_4 (pH = 1 and 2); (f) FE for H_2 in 0.5 M K_2SO_4 (pH = 1 and 2).

respectively. Compared to previously reported materials of the same type, such a high current density is at the forefront (Fig. S17, ESI†). Likewise, the XPS spectrum shown in Fig. S18, ESI† proves that the valence of Ni sites in NiPc-Im-COF is still maintained at +2 after the CO_2RR in all kinds of electrolytes. FE_{CO} kept over 90% for a duration of 6 hours when the CO_2RR was conducted in 5 M KOH at −0.6 V (Fig. S19, ESI†). At the same time, the PXRD patterns performed after the CO_2RR suggested that the structure of NiPc-Im-COF remained stable (Fig. S20, ESI†).

To improve the utilization of CO_2, CO_2RR for the robust NiPc-Im-COF was also performed in GDE with acidic electrolyte (0.5 M K_2SO_4, the pH value was adjusted to 1 and 2 by H_2SO_4). As shown in Fig. S21, ESI,† the total current density in K_2SO_4 (pH = 1) was higher than that in K_2SO_4 (pH = 2) and exhibited ion concentration dependence, with only a slight decrease in the selectivity for CO_2RR to CO. As illustrated in Fig. 5d, NiPc-Im-COF also exhibited high selectivity and the FE_{CO} exceeded 90% in K_2SO_4 (pH = 2) from −1.1 V to −1.4 V. When the pH was reduced to 1, FE_{CO} remained above 80% within the voltage range of −1.2 V to −1.4 V, and the maximum J_{CO} reached 87 mA cm^{-2} (Fig. 5e). The electrocatalytic CO_2RR was also carried out in H_2SO_4 (pH = 1 and 2) without added K_2SO_4, and the current density significantly decreased (Fig. S22, ESI†). Besides, the FE_{H2} was almost 100% in H_2SO_4 (Fig. 5f), demonstrating that the presence of K^+ in the electrolyte effectively suppressed the HER. The pH value was tested after CO_2RR. As shown in Fig. S23, ESI,† the pH values of electrolytes with K_2SO_4 (pH = 1 and 2) were unchanged, whereas the pH values of electrolytes without K_2SO_4 (pH = 1 and 2) changed to 1.7 and 2.4. The pH changes further confirmed the dominance of CO_2RR in the presence of K^+. The valence of Ni sites in NiPc-Im-COF and its crystallinity remained stable after CO_2RR, as confirmed by XPS and XRD (Fig. S24 and S25, ESI†). FE_{CO} remained stable (about 90%) for 6 hours at −1.3 V in K_2SO_4 (pH = 1) (Fig. S26, ESI†).

In order to gain a deeper insight into the mechanism of the electrocatalytic activity of NiPc-Im-COF, ^{13}C-labeled CO_2 isotope experiments through gas chromatography–mass spectrometry (GC-MS) at −0.8 V in $KH^{12}CO_3$ and KCl electrolytes were conducted. As shown in Fig. 6a and Fig. S27, ESI,† when the CO_2RR was conducted under ^{13}C-labeling CO_2 in 0.5 M $KH^{12}CO_3$, both the signals of ^{12}CO and ^{13}CO were observed. While only ^{13}CO was observed when $KH^{12}CO_3$ electrolyte was replaced by the KCl electrolyte. These results revealed that the source of carbon in the CO_2RR was the CO_2 dissolved in the $KHCO_3$ solution. Then, to confirm the intermediates during the CO_2RR, *in situ* attenuated total reflection Fourier transform infrared spectroscopy (ATR-FTIR) at −0.8 V in 0.5 M $KHCO_3$ was performed. As shown in Fig. 6b, the real-time FTIR spectra of CO_2RR on NiPc-Im-COF electrodes exhibited two prominent bands at 1400 and 2330–2360 cm^{-1}, which were assigned to the *COOH and adsorption of CO_2, respectively.[60,61] These results suggested that *COOH plays a crucial role as the key intermediate in the formation of CO.

Based on the results of isotope experiments and ATR-FTIR, density functional theory (DFT) calculations were conducted to calculate the free energies of reaction intermediates for CO_2RR and HER. In general, the pathway for the formation of CO can be summarized as the adsorption of CO_2 to form *CO_2, then the generation of *COOH and *CO through the process of electron-coupled proton transfer, and finally, the CO desorption from active sites. From the free energy diagram in Fig. 6c and d, the energy barrier of the *COOH formation decreases from 2.49 eV to 1.02 eV, while the energy barrier of the *H formation increases from −0.16 eV to 2.38 eV when an acidic solution containing K^+ is employed as electrolyte. The higher energy barrier of *H formation is consistent with the experimental results that CO is the major product for CO_2RR in acidic electrolytes with K^+.

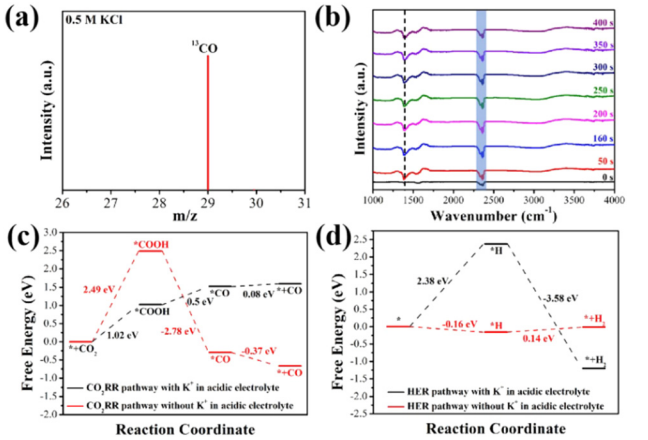

Fig. 6 (a) Mass spectra of CO in the $^{13}CO_2$-saturated 0.5 M KCl for NiPc-Im-COF; (b) *operando* ATR-FTIR of NiPc-Im-COF during CO_2RR at −0.8 V in 0.5 M $KHCO_3$; (c) free energy diagrams of NiPc-Im-COF for CO_2RR and (d) HER pathways with or without K^+ in acidic electrolyte.

Conclusions

In summary, the robust NiPc-Im-COF linked by irreversible covalent bonds was successfully prepared and employed as a highly efficient electrocatalyst for CO_2RR. It exhibited a remarkable CO selectivity exceeding 90% within a broad potential range of −0.7 to −1.1 V. Moreover, due to the brilliant stability of the NiPc-Im-COF conferred by the imidazole ring in alkaline and acid solutions, KOH and acidic K_2SO_4 solutions were employed as electrolytes in GDE to break through the limitation of CO_2 mass transfer. NiPc-Im-COF exhibited FE_{CO} exceeding 80% in KOH solutions of varying concentrations and the J_{CO} reached 267 mA cm^{-2} at −0.8 V in 5 M KOH. Furthermore, NiPc-Im-COF exhibited high efficiency in CO_2RR, with FE_{CO} exceeding 85% and a J_{CO} of 87 mA cm^{-2} at −1.4 V in acidic K_2SO_4 (pH = 1), effectively suppressing the hydrogen evolution reaction (HER). Crucially, the structure of NiPc-Im-COF and the valence of Ni sites can remain stable after CO_2RR, which is beneficial for the accessibility of active sites. Our work provides an effective strategy to enhance the stability of COFs through the linkage of the imidazole ring for CO_2RR. This approach can

shed light on the rational design of porous framework materials for the electrocatalytic CO_2RR in various environments.

Author contributions

X. Y., H. L., Y. H., and R. C. conceived the project and wrote the manuscript. X. Y. performed the experiments and collected the data. H. L., D. S., and Y. H. polished the manuscript. All authors discussed the results and commented on the manuscript.

Conflicts of interest

The authors declare that they have no conflict of interest.

Acknowledgements

The work was supported by the National Key Research and Development Program of China (2021YFA1501500, 2022YFA1-505700), NSFC (U22A20436, 22071245, 22033008, 22220102005, 22201286), and Fujian Science & Technology Innovation Laboratory for Optoelectronic Information of China (2021ZZ103), Open Science Promotion Plan 2023 of CSTCloud. The authors thank the beamline BL14W1 station for XAS measurements at the Shanghai Synchrotron Radiation Facility, China.

References

1 A. Eleni, E. H. John, K. M. Edgar, G. L. Foster, A. Ridgwell, G. N. Inglis, R. D. Pancost, D. J. Lunt and P. N. Pearson, Changing atmospheric CO_2 concentration was the primary driver of early Cenozoic climate, *Nature*, 2016, **533**, 380–384.

2 C. He, Y.-H. Zou, D.-H. Si, Z.-A. Chen, T.-F. Liu, R. Cao and Y.-B. Huang, A porous metal-organic cage liquid for sustainable CO_2 conversion reactions, *Nat. Commun.*, 2023, **14**, 3317.

3 J. Liang, Q. Wu, Y. B. Huang and R. Cao, Reticular frameworks and their derived materials for CO_2 conversion by thermo-catalysis, *EnergyChem*, 2021, **3**, 100064.

4 J. Chen, Y. Zha, B. Liu, Y. Li, Y. Xu and X. Liu, Rationally designed water enriched nano reactor for stable CO_2 hydrogenation with near 100% ethanol selectivity over diatomic palladium active sites, *ACS Catal.*, 2023, **13**, 7110–7121.

5 X. Feng, Y. Pi, Y. Song, C. Brzezinski, Z. Xu, Z. Li and W. Lin, Metal-Organic frameworks significantly enhance photocatalytic hydrogen evolution and CO_2 reduction with earth-abundant copper photosensitizers, *J. Am. Chem. Soc.*, 2020, **142**, 690–695.

6 C. He, D.-H. Si, Y.-B. Huang and R. Cao, A CO_2-masked carbene functionalized covalent organic framework for highly efficient carbon dioxide conversion, *Angew. Chem., Int. Ed.*, 2022, **61**, e202207478.

7 N. Li, J.-J. Liu, J.-W. Sun, B.-X. Dong, L.-Z. Dong, S.-J. Yao, Z. Xin, S.-L. Li and Y.-Q. Lan, Calix[8]arene-constructed stable polyoxo-titanium clusters for efficient CO_2 photoreduction, *Green Chem.*, 2020, **22**, 5325–5332.

8 N. Li, D.-H. Si, Q.-j Wu, Q. Wu, Y.-B. Huang and R. Cao, Boosting electrocatalytic CO_2 reduction with conjugated bimetallic Co/Zn polyphthalocyanine frameworks, *CCS Chem.*, 2023, **5**, 1130–1143.

9 C. H. Vo, C. Mondelli, H. Hamedi, J. Pérez-Ramírez, S. Farooq and I. A. Karimi, Sustainability assessment of thermocatalytic conversion of CO_2 to transportation fuels, Methanol, and 1-Propanol, *ACS Sustainable Chem. Eng.*, 2021, **9**, 10591–10600.

10 P. Zhang, X. Zhan, L. Xu, X. Fu, T. Zheng, X. Yang, Q. Xu, D. Wang, D. Qi, T. Sun and J. Jiang, Mass production of a single-atom cobalt photocatalyst for high-performance visible-light photocatalytic CO_2 reduction, *J. Mater. Chem. A*, 2021, **9**, 26286–26297.

11 C. Costentin, M. Robert and J.-M. Savéant, Catalysis of the electrochemical reduction of carbon dioxide, *Chem. Soc. Rev.*, 2013, **42**, 2423–2436.

12 S. Nitopi, E. Bertheussen, S. B. Scott, X. Liu, A. K. Engstfeld, S. Horch, B. Seger, I. E. L. Stephens, K. Chan, C. Hahn, J. K. Norskov, T. F. Jaramillo and I. Chorkendorff, Progress and perspectives of electrochemical CO_2 reduction on copper in aqueous electrolyte, *Chem. Rev.*, 2019, **119**, 7610–7672.

13 Z. Chen, A. Huang, K. Yu, T. Cui, Z. Zhuang, S. Liu, J. Li, R. Tu, K. Sun, X. Tan, J. Zhang, D. Liu, Y. Zhang, P. Jiang, Y. Pan, C. Chen, Q. Peng and Y. Li, Fe_1N_4-O_1 site with axial Fe-O coordination for highly selective CO_2 reduction over a wide potential range, *Energy Environ. Sci.*, 2021, **14**, 3430–3437.

14 G. Wu, Y. Song, Q. Zheng, C. Long, T. Fan, Z. Yang, X. Huang, Q. Li, Y. Sun, L. Zuo, S. Lei and Z. Tang, Selective electroreduction of CO_2 to n-Propanol in two-step tandem catalytic system, *Adv. Energy Mater.*, 2022, **12**, 2202054.

15 Q.-X. Li, D.-H. Si, W. Lin, Y.-B. Wang, H.-J. Zhu, Y.-B. Huang and R. Cao, Highly efficient electroreduction of CO_2 by defect single-atomic Ni-N_3 sites anchored on ordered micro-macroporous carbons, *Sci. China: Chem.*, 2022, **65**, 1584–1593.

16 F. Lü, H. Bao, F. He, G. Qi, J. Sun, S. Zhang, L. Zhuo, H. Yang, G. Hu, J. Luo and X. Liu, Nitrogen dopant induced highly selective CO_2 reduction over lotus-leaf shaped ZnO nanorods, *Mater. Chem. Front.*, 2021, **5**, 4225–4230.

17 P. Wei, D. Gao, T. Liu, H. Li, J. Sang, C. Wang, R. Cai, G. Wang and X. Bao, Coverage-driven selectivity switch from ethylene to acetate in high-rate CO_2/CO electrolysis, *Nat. Nanotechnol.*, 2023, **18**, 299–306.

18 C. Long, X. Liu, K. Wan, Y. Jiang, P. Wei, C. Yang, G. Wu, W. Wang, J. Guo, L. Li, K. Pang, Q. Li, C. Cui, S. Liu, T. Tan and Z. Tang, Regulating reconstruction of oxide-derived Cu for electrochemical CO_2 reduction toward n-propanol, *Sci. Adv.*, 2023, **9**, eadi6119.

19 Y. Yan, L. Ke, Y. Ding, Y. Zhang, K. Rui, H. Lin and J. Zhu, Recent advances in Cu-based catalysts for electroreduction of carbon dioxide, *Mater. Chem. Front.*, 2021, **5**, 2668–2683.

20 J. Sang, P. Wei, T. Liu, H. Lv, X. Ni, D. Gao, J. Zhang, H. Li, Y. Zang, F. Yang, Z. Liu, G. Wang and X. Bao, A reconstructed $Cu_2P_2O_7$ catalyst for selective CO_2 electroreduction to multicarbon, *Angew. Chem., Int. Ed.*, 2022, **61**, e202114238.

21 J. Zhang, G. Zeng, S. Zhu, H. Tao, Y. Pan, W. Lai, J. Bao, C. Lian, D. Su, M. Shao and H. Huang, Steering CO_2 electroreduction pathway toward ethanol *via* surface-bounded hydroxyl species-induced noncovalent interaction, *Proc. Natl. Acad. Sci. U. S. A.*, 2023, **120**, e2218987120.

22 Y. Zhou, F. Che, M. Liu, C. Zou, Z. Liang, P. De Luna, H. Yuan, J. Li, Z. Wang, H. Xie, H. Li, P. Chen, E. Bladt, R. Quintero-Bermudez, T.-K. Sham, S. Bals, J. Hofkens, D. Sinton, G. Chen and E. H. Sargent, Dopant-induced electron localization drives CO_2 reduction to C_2 hydrocarbons, *Nat. Chem.*, 2018, **10**, 974–980.

23 J. Dong, Y. Liu, J. Pei, H. Li, S. Ji, L. Shi, Y. Zhang, C. Li, C. Tang, J. Liao, S. Xu, H. Zhang, Q. Li and S. Zhao, Continuous electroproduction of formate *via* CO_2 reduction on local symmetry-broken single-atom catalysts, *Nat. Commun.*, 2023, **14**, 6849.

24 S. Garg, M. Li, A. Z. Weber, L. Ge, L. Li, V. Rudolph, G. Wang and T. E. Rufford, Advances and challenges in electrochemical CO_2 reduction processes: an engineering and design perspective looking beyond new catalyst materials, *J. Mater. Chem. A*, 2020, **8**, 1511–1544.

25 N. Kornienko, Y. Zhao, C. S. Kley, C. Zhu, D. Kim, S. Lin, C. J. Chang, O. M. Yaghi and P. Yang, Metal-Organic frameworks for electrocatalytic reduction of carbon dioxide, *J. Am. Chem. Soc.*, 2015, **137**, 14129–14135.

26 C. Yan, H. Li, Y. Ye, H. Wu, F. Cai, R. Si, J. Xiao, S. Miao, S. Xie, F. Yang, Y. Li, G. Wang and X. Bao, Coordinatively unsaturated nickel-nitrogen sites towards selective and high-rate CO_2 electroreduction, *Energy Environ. Sci.*, 2018, **11**, 1204–1210.

27 L. Zhang, Z. J. Zhao and J. Gong, Nanostructured materials for heterogeneous electrocatalytic CO_2 reduction and their related reaction mechanisms, *Angew. Chem., Int. Ed.*, 2017, **56**, 11326–11353.

28 B. Li, H. Ou, S. Chen, Y.-Q. Su and D. Wang, Recent Advances in CO_2 Reduction Reaction to Value-added C1 Products by Single-atom Catalysts, *Chem. Res. Chin. Univ.*, 2023, **39**, 527–544.

29 Y. Mao, S. Chen, Z. Jia, X. Dong and Q. Mao, CV-etched Nanostructured Ag Foils for Efficient Electrochemical CO_2 Reduction, *Chem. Res. Chin. Univ.*, 2023, **39**, 1031–1036.

30 M. E. Leonard, L. E. Clarke, A. Forner-Cuenca, S. M. Brown and F. R. Brushett, Investigating electrode flooding in a flowing electrolyte, gas-fed carbon dioxide electrolyzer, *ChemSusChem*, 2020, **13**, 400–411.

31 C. S. Diercks, Y. Liu, K. E. Cordova and O. M. Yaghi, The role of reticular chemistry in the design of CO_2 reduction catalysts, *Nat. Mater.*, 2018, **17**, 301–307.

32 Z. Liang, H.-Y. Wang, H. Zheng, W. Zhang and R. Cao, Porphyrin-based frameworks for oxygen electrocatalysis and catalytic reduction of carbon dioxide, *Chem. Soc. Rev.*, 2021, **50**, 2540–2581.

33 C. Wang, Z. Lv, W. Yang, X. Feng and B. Wang, A rational design of functional porous frameworks for electrocatalytic CO_2 reduction reaction, *Chem. Soc. Rev.*, 2023, **52**, 1382–1427.

34 J. Wang, H. Hu, S. Lu, J. Hu, H. Zhu, F. Duan and M. Du, Conductive metal and covalent organic frameworks for electrocatalysis: design principles, recent progress and perspective, *Nanoscale*, 2022, **14**, 277–288.

35 Q.-J. Wu, J. Liang, Y.-B. Huang and R. Cao, Thermo-, electro-, and photocatalytic CO_2 conversion to value-added products over porous metal/covalent organic frameworks, *Acc. Chem. Res.*, 2022, **55**, 2978–2997.

36 A. P. Côté, A. I. Benin, N. W. Ockwig, M. O'Keeffe, A. J. Matzger and O. M. Yaghi, Porous, crystalline, covalent organic frameworks, *Science*, 2005, **310**, 1166–1170.

37 P. J. Waller, F. Gándara and O. M. Yaghi, Chemistry of covalent organic frameworks, *Acc. Chem. Res.*, 2015, **48**, 3053–3063.

38 Q. Wu, M. J. Mao, Q. J. Wu, J. Liang, Y. B. Huang and R. Cao, Construction of donor-acceptor heterojunctions in covalent organic framework for enhanced CO_2 electroreduction, *Small*, 2021, **17**, e2004933.

39 Q. Wu, R.-K. Xie, M.-J. Mao, G.-L. Chai, J.-D. Yi, S.-S. Zhao, Y.-B. Huang and R. Cao, Integration of strong electron transporter tetrathiafulvalene into metalloporphyrin-based covalent organic framework for highly efficient electroreduction of CO_2, *ACS Energy Lett.*, 2020, **5**, 1005–1012.

40 X. Zhang, Y.-Z. Yuan, H.-F. Li, Q.-J. Wu, H.-J. Zhu, Y.-L. Dong, Q. Wu, Y.-B. Huang and R. Cao, Viologen linker as a strong electron-transfer mediator in the covalent organic framework to enhance electrocatalytic CO_2 reduction, *Mater. Chem. Front.*, 2023, **7**, 2661–2670.

41 E. Jin, M. Asada, Q. Xu, S. Dalapati, M. A. Addicoat, M. A. Brady, H. Xu, T. Nakamura, T. Heine, Q. Chen and D. Jiang, Two-dimensional sp^2 carbon-conjugated covalent organic frameworks, *Science*, 2017, **357**, 673–676.

42 X.-N. Feng, Y. Yang, X. Cao, T. Wang, D.-M. Kong, X.-B. Yin, B. Li and X.-H. Bu, General approach to construct C–C single bond-linked covalent organic frameworks, *J. Am. Chem. Soc.*, 2023, **145**, 21284–21292.

43 B. Zhang, M. Wei, H. Mao, X. Pei, S. A. Alshmimri, J. A. Reimer and O. M. Yaghi, Crystalline dioxin-linked covalent organic frameworks from irreversible reactions, *J. Am. Chem. Soc.*, 2018, **140**, 12715–12719.

44 J. Liu, T. Yang, Z.-P. Wang, P.-L. Wang, J. Feng, S.-Y. Ding and W. Wang, Pyrimidazole-based covalent organic frameworks: integrating functionality and ultrastability *via* isocyanide chemistry, *J. Am. Chem. Soc.*, 2020, **142**, 20956–20961.

45 P.-F. Wei, M.-Z. Qi, Z.-P. Wang, S.-Y. Ding, W. Yu, Q. Liu, L.-K. Wang, H.-Z. Wang, W.-K. An and W. Wang, Benzoxazole-linked ultrastable covalent organic frameworks for photocatalysis, *J. Am. Chem. Soc.*, 2018, **140**, 4623–4631.

46 J. Guo, Y. Xu, S. Jin, L. Chen, T. Kaji, Y. Honsho, M. A. Addicoat, J. Kim, A. Saeki, H. Ihee, S. Seki, S. Irle, M. Hiramoto, J. Gao and D. Jiang, Conjugated organic framework with three-dimensionally ordered stable structure and delocalized π clouds, *Nat. Commun.*, 2013, **4**, 2736.

47 M. Wang, M. Ballabio, M. Wang, H.-H. Lin, B. P. Biswal, X. Han, S. Paasch, E. Brunner, P. Liu, M. Chen, M. Bonn, T. Heine, S. Zhou, E. Cánovas, R. Dong and X. Feng, Unveiling electronic properties in metal-phthalocyanine-based pyrazine-linked conjugated two-dimensional covalent organic frameworks, *J. Am. Chem. Soc.*, 2019, **141**, 16810–16816.

48 Q. Zhang, F. Zhang, J. Dong, M. Shao, M. Zhu, D. Wang, Y. Guo, J. Zhang and Y. Liu, Controlling the nucleation process to prepare a family of crystalline tribenzimidazole-based covalent organic frameworks, *Chem. Mater.*, 2022, **34**, 6977–6984.

49 Z. Meng, R. M. Stolz and K. A. Mirica, Two-dimensional chemiresistive covalent organic framework with high intrinsic conductivity, *J. Am. Chem. Soc.*, 2019, **141**, 11929–11937.

50 H. Zhong, K. H. Ly, M. Wang, Y. Krupskaya, X. Han, J. Zhang, J. Zhang, V. Kataev, B. Büchner, I. M. Weidinger, S. Kaskel, P. Liu, M. Chen, R. Dong and X. Feng, Phthalocyanine-based layered two-dimensional conjugated metal-organic framework as highly efficient electrocatalyst for oxygen reduction reaction, *Angew. Chem., Int. Ed.*, 2019, **58**, 10677–10682.

51 Y. Liu, C. Li, C. Tan, Z. Pei, T. Yang, S. Zhang, Q. Huang, Y. Wang, Z. Zhou, X. Liao, J. Dong, H. Tan, W. Yan, H. Yin, Z.-Q. Liu, J. Huang and S. Zhao, Electrosynthesis of chlorine from seawater-like solution through single-atom catalysts, *Nat. Commun.*, 2023, **14**, 2475.

52 X. Han, T. Zhang, X. Wang, Z. Zhang, Y. Li, Y. Qin, B. Wang, A. Han and J. Liu, Hollow mesoporous atomically dispersed metal-nitrogen-carbon catalysts with enhanced diffusion for catalysis involving larger molecules, *Nat. Commun.*, 2022, **13**, 2900.

53 L. Lai, J. R. Potts, D. Zhan, L. Wang, C. K. Poh, C. Tang, H. Gong, Z. Shen, J. Lin and R. S. Ruoff, Exploration of the active center structure of nitrogen-doped graphene-based catalysts for oxygen reduction reaction, *Energy Environ. Sci.*, 2012, **5**, 7936.

54 Z. Meng, A. Aykanat and K. A. Mirica, Welding metallophthalocyanines into bimetallic molecular meshes for ultrasensitive, low-power chemiresistive detection of gases, *J. Am. Chem. Soc.*, 2018, **141**, 2046–2053.

55 F. Pan, H. Zhang, Z. Liu, D. Cullen, K. Liu, K. More, G. Wu, G. Wang and Y. Li, Atomic-level active sites of efficient imidazolate framework-derived nickel catalysts for CO_2 reduction, *J. Mater. Chem. A*, 2019, **7**, 26231–26237.

56 S. Wu, H. Chen, C. Jia, L. Liao, K. Chen, S. Ci, Q. Xu and Z. Wen, Bifunctional electroreduction catalysts of NiFe alloy on N-doped carbon toward industrial-level CO_2 conversion powered by Zn-air batteries, *Inorg. Chem. Front.*, 2023, **10**, 4484–4495.

57 T. Zheng, K. Jiang, N. Ta, Y. Hu, J. Zeng, J. Liu and H. Wang, Large-scale and highly selective CO_2 electrocatalytic reduction on nickel single-atom catalyst, *Joule*, 2019, **3**, 265–278.

58 N. Han, Y. Wang, L. Ma, J. Wen, J. Li, H. Zheng, K. Nie, X. Wang, F. Zhao, Y. Li, J. Fan, J. Zhong, T. Wu, D. J. Miller, J. Lu, S.-T. Lee and Y. Li, Supported cobalt polyphthalocyanine for high-performance electrocatalytic CO_2 reduction, *Chem.*, 2017, **3**, 652–664.

59 D. M. Koshy, S. Chen, D. U. Lee, M. B. Stevens, A. M. Abdellah, S. M. Dull, G. Chen, D. Nordlund, A. Gallo, C. Hahn, D. C. Higgins, Z. Bao and T. F. Jaramillo, Understanding the origin of highly selective CO2 electroreduction to CO on Ni, N-doped carbon catalysts, *Angew. Chem., Int. Ed.*, 2020, **59**, 4043–4050.

60 N. J. Firet and W. A. Smith, Probing the reaction mechanism of CO_2 electroreduction over Ag films *via* operando infrared spectroscopy, *ACS Catal.*, 2016, **7**, 606–612.

61 Q.-J. Wu, D. Si, Q. Wu, Y. Dong, R. Cao and Y.-B. Huang, Boosting Electroreduction of CO_2 over Cationic Covalent Organic Frameworks: Hydrogen Bonding Effects of Halogen Ions, *Angew. Chem., Int. Ed.*, 2023, **62**, e202215687.

